


Cite this: *RSC Adv.*, 2023, 13, 12634

# The supercapattery designed with a binary composite of niobium silver sulfide (NbAg<sub>2</sub>S) and activated carbon for enhanced electrochemical performance†

Hirra Rafique,<sup>a</sup> Muhammad Waqas Iqbal,<sup>id</sup> \*<sup>a</sup> Saikh Mohammad Wabaidur,<sup>b</sup> Haseeb ul Hassan,<sup>a</sup> Amir Muhammad Afzal,<sup>a</sup> Tasawar Abbas,<sup>a</sup> Mohamed A. Habila<sup>id</sup> <sup>b</sup> and Ehsan Elahi<sup>id</sup> <sup>c</sup>

A supercapattery is a hybrid device that is a combination of a battery and a capacitor. Niobium sulfide (NbS), silver sulfide (Ag<sub>2</sub>S), and niobium silver sulfide (NbAg<sub>2</sub>S) were synthesized by a simple hydrothermal method. NbAg<sub>2</sub>S (50/50 wt% ratio) had a specific capacity of 654 C g<sup>-1</sup>, which was higher than the combined specific capacities of NbS (440 C g<sup>-1</sup>) and Ag<sub>2</sub>S (232 C g<sup>-1</sup>), as determined by the electrochemical investigation of a three-cell assembly. Activated carbon and NbAg<sub>2</sub>S were combined to develop the asymmetric device (NbAg<sub>2</sub>S//AC). A maximum specific capacity of 142 C g<sup>-1</sup> was delivered by the supercapattery (NbAg<sub>2</sub>S//AC). The supercapattery (NbAg<sub>2</sub>S//AC) provided 43.06 W h kg<sup>-1</sup> energy density while retaining 750 W kg<sup>-1</sup> power density. The stability of the NbAg<sub>2</sub>S//AC device was evaluated by subjecting it to 5000 cycles. After 5000 cycles, the (NbAg<sub>2</sub>S//AC) device still had 93% of its initial capacity. This research indicates that merging NbS and Ag<sub>2</sub>S (50/50 wt% ratio) may be the best choice for future energy storage technologies.

Received 23rd February 2023  
Accepted 17th April 2023

DOI: 10.1039/d3ra01230a

rsc.li/rsc-advances

## 1. Introduction

The requirement for energy is increasing rapidly due to the increasing population with each passing day.<sup>1</sup> The energy produced by traditional methods can no longer meet the energy needs of modern society, so that is why new methods are being developed to generate and implements energy.<sup>2–4</sup> Energy storage devices are essential along with renewable energy resources for the continuous supply of energy. Traditional energy storage devices include batteries and capacitors. Supercapacitors (SCs) are an intermediate point between capacitors and conventional batteries.<sup>5,6</sup> The energy densities of Li-ion batteries (LIBs) reached 150 to 200 W h kg<sup>-1</sup>,<sup>7,8</sup> which are significantly higher compared to other battery types, such as Ni–Cd<sup>9,10</sup> Ni–MH,<sup>9</sup> and lead batteries.<sup>9</sup> Applications for electric vehicles are now feasible thanks to SCs with high power densities, longer life cycles, and fast charging.<sup>11</sup> SCs are cheaper than batteries and provide good power with a moderate energy density.<sup>12–14</sup> The SCs are considered a main electrical energy storage EES because of

their good energy and power densities.<sup>10,11,15–18</sup> According to their storing method, SCs are further divided into PCs (pseudo capacitors) and EDLCs (electric double-layer capacitors). Metal sulfide and conductive polymers are the most frequently used for PCs because of their electrochemical properties.<sup>19–21</sup> Owing to a shortage of energy production, electrical energy storage systems are being modified to meet energy requirements. This issue was solved by combining the characteristics of batteries and supercapacitors in a single hybrid device.<sup>22</sup> Supercapatteries are hybrid devices that utilize both a capacitive electrode and a battery electrode.<sup>23</sup> Compared to the present LIBs, supercapacitors, and supercapatteries have shown a reasonable potential for energy and power density.<sup>11</sup> Supercapatteries have a substantially greater energy density than supercapacitors.<sup>24–27</sup> Layered and non-layered sulfides are the two primary groups into which the metal sulfides (MSs) can be separated. Non-layered metal sulfide MSs with high theoretical capacities are FeS<sub>2</sub>, NiS<sub>2</sub>, CoS<sub>2</sub>, and MnS. They are also commonly accessible, cost-effective, and environmentally friendly.<sup>28–30</sup> Covalent bonds in semi-metal sulfides join the layers to form the layered MSs, including MoS<sub>2</sub>, WS<sub>2</sub>, SnS<sub>2</sub>, VS<sub>2</sub>, and many others.<sup>31–36</sup> Changing morphologies, sizes, structures, and compositions makes it possible to change the electrochemical properties of MSs.<sup>37,38</sup> Layered transition metal dichalcogenides (TMDs) with the structural formula MX<sub>2</sub> have gained a lot of attention due to their huge potential for energy

<sup>a</sup>Department of Physics, Riphah International University, Campus Lahore, Pakistan.  
E-mail: waqas.iqbal@riphah.edu.pk

<sup>b</sup>Chemistry Department, College of Science, King Saud University, Riyadh 11451, Saudi Arabia

<sup>c</sup>Department of Physics and Astronomy, Sejong University, Seoul, South Korea

† Electronic supplementary information (ESI) available. See DOI: <https://doi.org/10.1039/d3ra01230a>



storage applications.<sup>39</sup> In  $\text{MX}_2$ , X stands for Se, Te, S, and M denotes transition metal element.<sup>40</sup> Because of its excellent electrical conductivity, higher specific capacity, and long cycle life, NbS has become more popular as an anode material.<sup>41</sup> Liao *et al.* studied the use of Nb oxides for advanced hybrid capacitors. But still, there is a lot of work needed on Nb-based electrode material for SCs.<sup>42</sup> Niobium (Nb)-based materials have incredible potential for use in supercapacitors (SCs). However, the conductivity of niobium may be successfully increased by merging Nb with two metals. Niobium sulfide has excellent flexibility, hardness, electrical conductivity, long cycle life, high energy storage capacity, and extraordinary electrochemical properties.<sup>43</sup> Silver sulfide ( $\text{Ag}_2\text{S}$ ) nanomaterial is commonly utilized in batteries, thermoelectric sensors, infrared finders, photovoltaic cells, and conductors.<sup>44</sup> The ellipsoidal-shaped  $\text{Ag}_2\text{S}$  nano crystals size range lies from 5 to 20 nm.<sup>45</sup> According to Pawar *et al.*,  $\text{Ag}_2\text{S}$  had a high specific capacity, greater chemical and electrical conductivity, and is naturally abundant.<sup>46,47</sup>

In this work, we successfully synthesized niobium silver sulfide ( $\text{NbAg}_2\text{S}$ ) nanoparticles using a hydrothermal technique. The surface morphology and structural analysis of  $\text{NbAg}_2\text{S}$  were measured with a scanning electron-microscope (SEM) and X-ray diffraction (XRD). The  $\text{NbAg}_2\text{S}$  was electrochemically evaluated using cyclic voltammetry (CV), electrochemical-impedance-spectroscopy (EIS), and galvanostatic charge-discharge (GCD). The electrolyte used for testing was 1 M KOH. In addition, the  $\text{NbAg}_2\text{S}$  and activated carbon were combined to develop the supercapattery. The stability experiments were also performed to examine the coulombic efficiency and capacity retention of the  $\text{NbAg}_2\text{S}/\text{AC}$  device after 5000 cycles.

## 2. Experimental section

### 2.1. Materials

The subsequent materials were bought from Sigma Aldrich: carbon black (CB), niobium nitrate ( $\text{Nb}(\text{NO}_3)_5$ ), KOH pellets, silver nitrate ( $\text{AgNO}_3$ ), hydrochloric acid (HCl), activated carbon, sodium sulfide hydrate ( $\text{Na}_2\text{S} \cdot 9\text{H}_2\text{O}$ ) and niobium nitrate ( $\text{Nb}(\text{NO}_3)_5$ ). The chemicals were bought in their purest form and weren't further purified before use. Deionized water (DIW) was used to make solutions, wash samples, and prepare electrolytes. The reference electrodes ( $\text{Hg}/\text{HgO}$ ), nickel foam, and platinum wire were imported from Japan.

### 2.2. Material synthesis

Niobium sulfide was first made using a hydrothermal technique. The hydrothermal method was chosen because of its ease and simplicity.<sup>47</sup> 0.8 M (2.32 g) of  $\text{Nb}(\text{NO}_3)_5$  and 0.8 M (0.6243 g) of  $\text{Na}_2\text{S} \cdot 9\text{H}_2\text{O}$  were dissolved in 10 ml of DIW to synthesize NbS.  $\text{Na}_2\text{S}$  solution was added to the niobium nitrate solution and placed on a hot magnetic stirrer. After 40 min of continuous stirring, the prepared solution was put into an autoclave. It was then placed in a furnace at 160 °C for 8 h. To remove the impurities, solutions were washed several times with DIW and ethanol. After complete washing, the prepared material was transferred to the dry dish and placed inside the oven to dry at 60 °C for 3 h. After completely following the above procedure, the material was finally grinded with the use of a hand grinder and collected inside the dry bottle, and collected at room temperature.

The silver sulfide nanoparticles were made using the previously mentioned procedures. Similarly, we prepared 0.8 M of

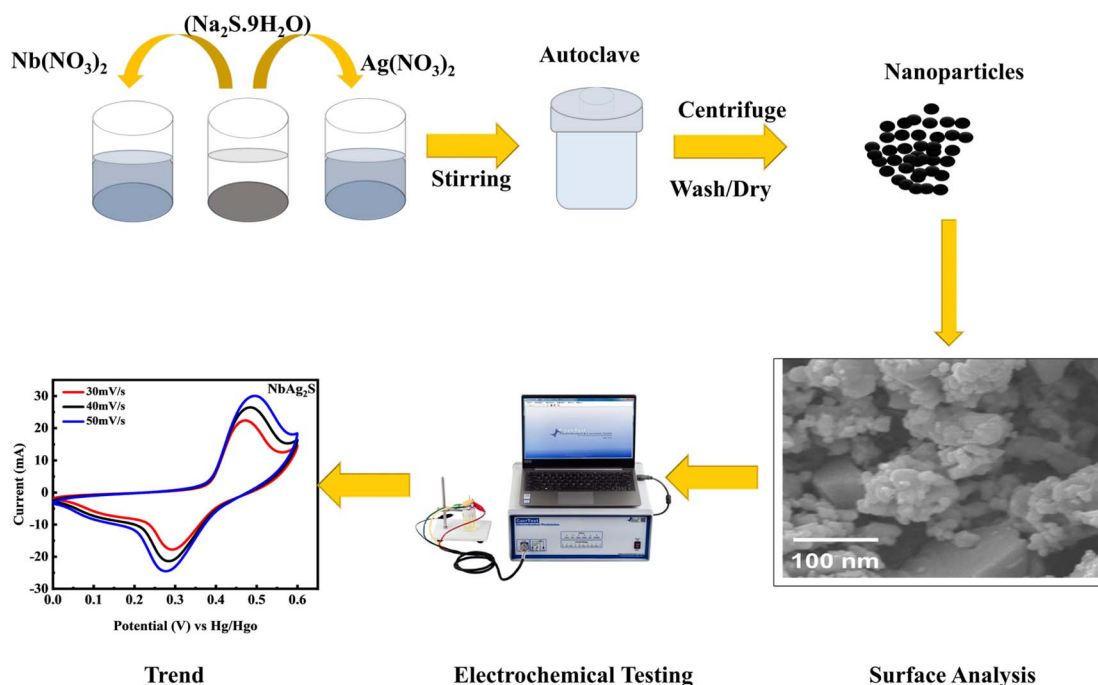


Fig. 1 Systematic illustration of the hydrothermal process and electrochemical testing.

sodium sulfide hydrate (0.6243 g) and silver nitrate (1.6987 g) solution in 10 ml of DIW to make silver sulfide. The sodium sulfide hydrate ( $\text{Na}_2\text{S} \cdot 9\text{H}_2\text{O}$ ) solution was transferred to the silver sulfide solution ( $\text{AgNO}_3$ ). The combined solution was continuously stirred for 60 min. The addition of  $\text{Na}_2\text{S} \cdot 9\text{H}_2\text{O}$  into  $\text{AgNO}_3$  turned the white solution black. The complete ready solution was then put into a 100 ml autoclave and was heated at 160 °C for 8 h before being permitted to cool at room temperature.

Niobium silver sulfide (50/50 wt% ratio) was formed similarly by making three different solutions. First, a 0.4 M (0.849 g) solution of silver nitrate was produced in 10 ml of DIW. 0.4 M (1.08 g) of niobium nitrate was used to make solution 2, while 0.8 M (0.6243 g) of sodium sulfide was used to make solution 3. Silver nitrate solution was placed on a hot plate, and the other two solutions were mixed drop by drop. Then, the procedure outlined above is completed to synthesize niobium silver sulfide. The illustration of synthesizing  $\text{NbAg}_2\text{S}$  through a hydrothermal process was displayed in Fig. 1.

### 2.3. Electrochemical measurement

Using cyclic voltammetry (CV), galvanostatic charge–discharge (GCD), and electrochemical impedance spectroscopy (EIS), the performance of  $\text{NbS}$ ,  $\text{Ag}_2\text{S}$ , and  $\text{NbAg}_2\text{S}$  was analyzed. The active material was first deposited on nickel foam (NF) and used as the working electrode. The counter electrode was platinum wire, and the reference electrode was  $\text{Hg}/\text{HgO}$ . A 1 M KOH solution was provided as the electrolyte during the entire electrochemical tests and was kept in a standard cell at room

temperature. The slurry was made with 15% ethylene black, 75% active material, and 10% PVDF binder. A homogeneous solution was prepared by continuously stirring for 6 h. It was then coated onto the NF. The NF was washed with HCl, ethanol, and DIW for further testing. The active substance was applied to a  $1 \times 1 \text{ cm}^2$  area of NF. For  $\text{NbS}$ ,  $\text{Ag}_2\text{S}$ , and  $\text{AgNb}_2\text{S}$ , the total weight of the active material transferred onto NF was close to 5–7 mg.

Further, binary composite ( $\text{NbAg}_2\text{S}$ ) and activated carbon were used as positive and negative electrodes for the supercapattery application. In the two-electrode assembly, 10 mg of active mass is transferred onto the NF. To reduce the NF effect, the AC was carefully coated on both sides of NF. The capacity from CV and GCD curves were measured for  $\text{NbS}$ ,  $\text{Ag}_2\text{S}$ , and  $\text{NbAg}_2\text{S}$ . The current density was maintained between 0.8 and  $2.0 \text{ A g}^{-1}$ . Additionally, the stability of this hybrid device was tested at room temperature using rapid test methods. With the help of the following equation, the specific capacity *via* CV curves for  $\text{NbS}$ ,  $\text{Ag}_2\text{S}$ , and  $\text{NbAg}_2\text{S}$  was determined.<sup>48–50</sup>

$$Q_s = \frac{1}{mv} \int_{V_i}^{V_f} I \times V dV \quad (1)$$

The area is represented by  $\int_{V_i}^{V_f} I \times V dV$ , the active mass is  $m$ , and the scanning speed is  $v$ . The equation below can be applied to measure the capacity through GCD.<sup>51</sup>

$$Q_s = \frac{I \times t}{m} \quad (2)$$

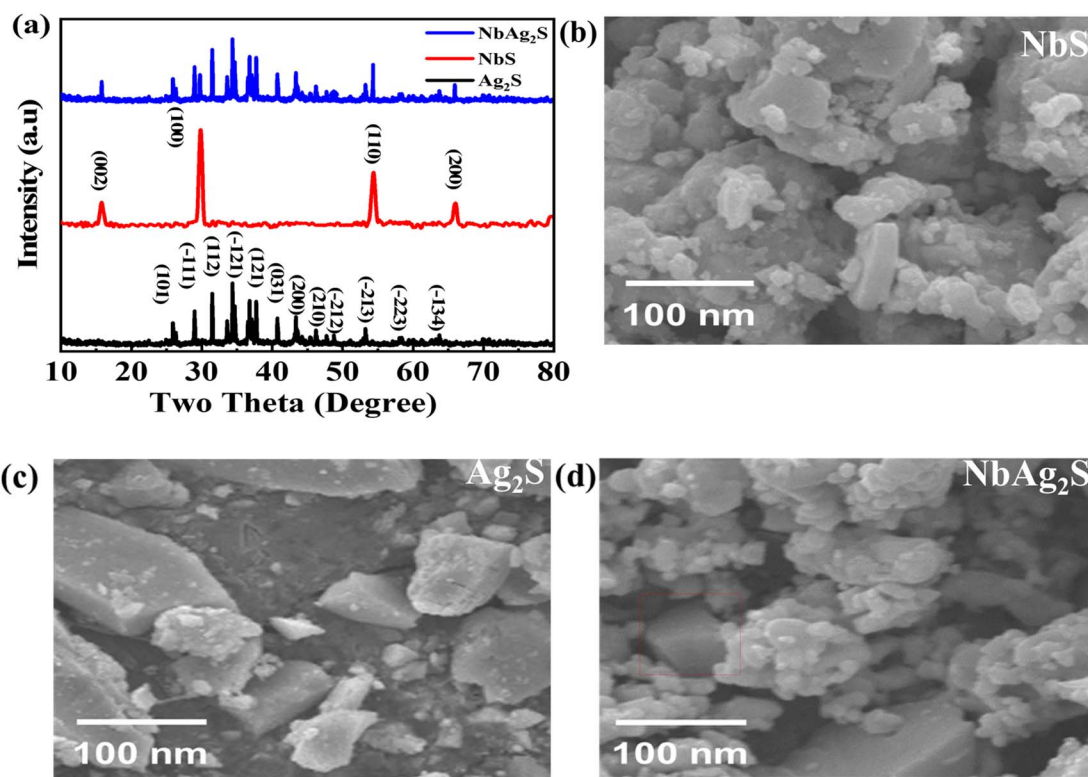


Fig. 2 (a) XRD pattern for  $\text{Ag}_2\text{S}$ ,  $\text{NbS}$ , and  $\text{Ag}_2\text{NbS}$ . (b–d) SEM images for  $\text{NbS}$ ,  $\text{Ag}_2\text{S}$ , and  $\text{NbAg}_2\text{S}$ , respectively.



The discharge time is indicated by “ $t$ ” and the current is denoted by “ $I$ .”

The following equations determined energy and power density for NbS, Ag<sub>2</sub>S, and NbAg<sub>2</sub>S.<sup>51</sup>

$$E = \frac{Q \times \Delta V}{2 \times 3.6} \quad (3)$$

$$P = \frac{E \times 3600}{\Delta t} \quad (4)$$

$E$  shows energy density,  $Q$  represents capacity, the operating potential is indicated by  $V$ ,  $t$  is the discharge time, and  $P$  is the power density.

### 3. Results and discussion

#### 3.1. X-ray diffraction analysis

To study the crystallinity, X-ray diffraction (XRD) was used. Fig. 2(a) indicates the XRD pattern for NbS, Ag<sub>2</sub>S, and NbAg<sub>2</sub>S. Scherer's equation was used to determine the size of the crystallite

$$D = \frac{k\lambda}{\beta \cos \theta} \quad (5)$$

In this equation  $D$  means the crystallite size,  $\lambda$  is the wavelength, and  $\beta$  is the full-width half maxima. The typical size for Ag<sub>2</sub>S was 20 nm, NbS was 23 nm, and NbAg<sub>2</sub>S was 26 nm from XRD data. The XRD pattern for Ag<sub>2</sub>S displays peaks related to (101), ( $\bar{1}$ 11), (112), ( $\bar{1}$ 21), (121), (031), (200), (210), ( $\bar{2}$ 12), ( $\bar{2}$ 13), ( $\bar{2}$ 23) and ( $\bar{1}$ 34), planes which match with the JCPDF-014-0072-Ag<sub>2</sub>S.<sup>52</sup> The planes are centered at  $2\theta = 26.3^\circ$ ,  $30.1^\circ$ ,  $31.04^\circ$ ,  $34.6^\circ$ ,  $36.7^\circ$ ,  $37.8^\circ$ ,  $40.7^\circ$ ,  $43.6^\circ$ ,  $48.6^\circ$ ,  $53.2^\circ$ , and  $57.9^\circ$ , respectively. The peaks for NbS were related to (002), (100), (110), and (200) planes, matched with JCPDF-01-089-5008.<sup>53</sup> The NbAg<sub>2</sub>S was also analyzed using the XRD. The XRD pattern for NbAg<sub>2</sub>S matches with the NbS and Ag<sub>2</sub>S XRD spikes confirming the successful formation of NbAg<sub>2</sub>S.<sup>45,54</sup>

#### 3.2. Scanning electron microscope (SEM)

The morphological characteristics of NbS, Ag<sub>2</sub>S, and NbAg<sub>2</sub>S were analyzed using scanning electron microscopy (SEM). Fig. 2(b) displayed the SEM image of NbS<sub>2</sub>; Fig. 2(c) presented the SEM image of Ag<sub>2</sub>S, and Fig. 2(d) presented the SEM image of NbAg<sub>2</sub>S. As can be observed from these images both Ag<sub>2</sub>S and NbS consisted of small nanoparticles. The morphology NbS and Ag<sub>2</sub>S indicated the crystalline structure. Above their crystalline structure, some amorphous structure was found. This was due to the presence of sulfide ions. Pure metals like Nb and Ag

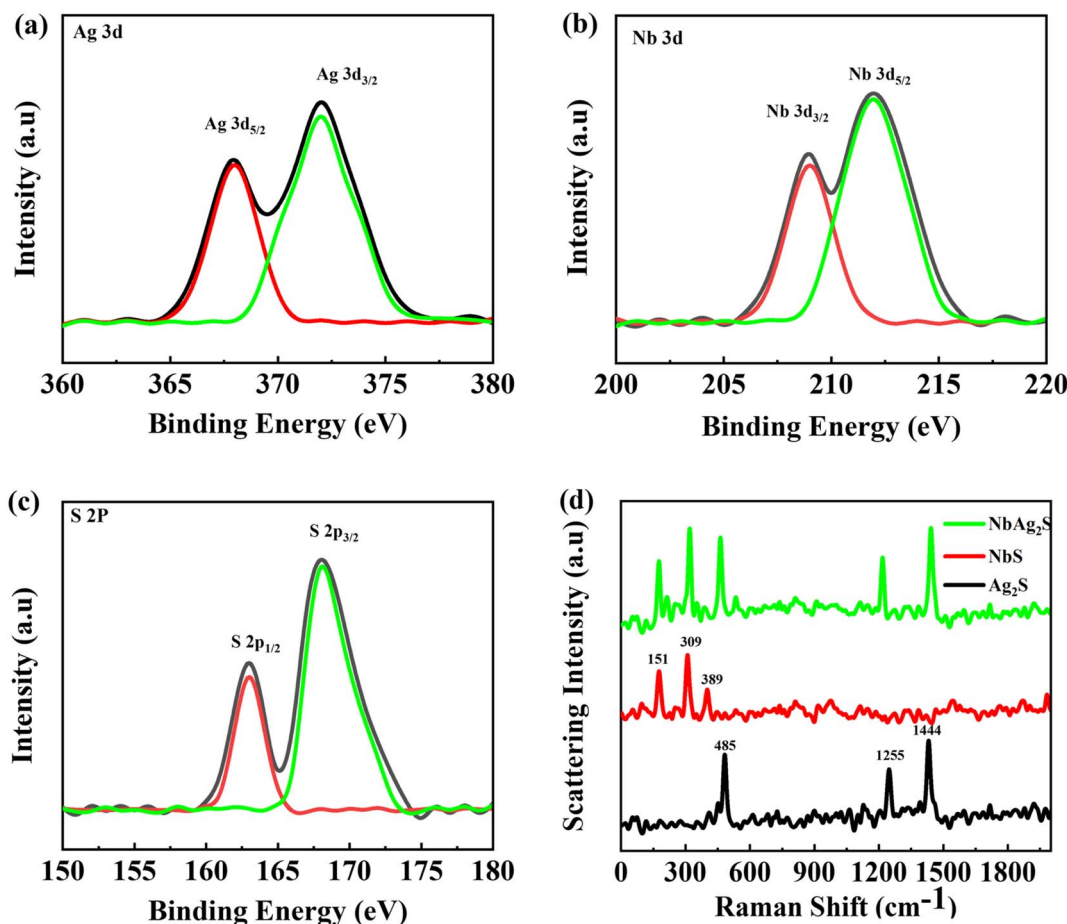


Fig. 3 (a–c) XPS spectrum for Ag 3d, Nb 3d, and S 2p, respectively. (d) Raman spectrometry for Ag<sub>2</sub>S, NbS, and NbAg<sub>2</sub>S.





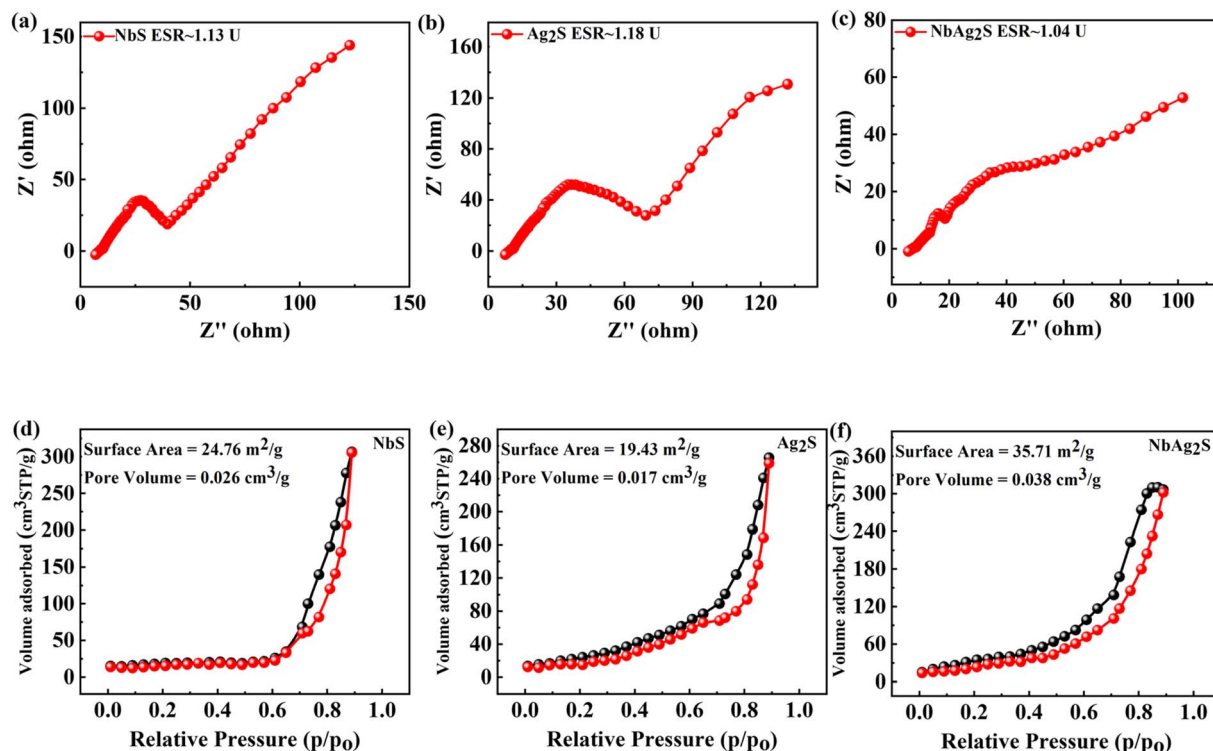


Fig. 4 (a–c) EIS calculation for NbS, Ag<sub>2</sub>S, and NbAg<sub>2</sub>S, respectively. (d–f) BET calculation for NbS, Ag<sub>2</sub>S, and NbAg<sub>2</sub>S, respectively.

Table 1 Specific parameters calculated through BET measurements for NbS, Ag<sub>2</sub>S, and NbAg<sub>2</sub>S

Materials	Surface area (m <sup>2</sup> g <sup>−1</sup> )	Pore size (nm)	Pore volume (cm <sup>3</sup> g <sup>−1</sup> )
NbS	24.76	0.23	0.026
Ag <sub>2</sub> S	19.43	0.18	0.017
NbAg <sub>2</sub> S	35.71	0.23	0.038

showed crystalline form while the sulfur developed on the surface of these metals as observed from the SEM images is responsible for their amorphous nature. The amorphous structure was able to store more charge as compared to crystalline. The morphology of NbAg<sub>2</sub>S was shown in Fig. 2(d), showing a matrix composite with numerous active sites. Thus electrical conductivity and specific capacity of this NbAg<sub>2</sub>S were improved.

### 3.3. XPS analysis

By using X-ray photoelectron spectroscopy, the valence state of Ag, Nb, and S in the composite sample was calculated, as shown in Fig. 3(a–c). The XPS spectra for Ag in Fig. 3(a) revealed two unique peaks with a 5 eV gap between them. Ag 3d<sub>5/2</sub> appeared at 367.5 eV and the Ag 3d<sub>3/2</sub> appeared at 372.5 eV, both of which match with Ag<sup>+</sup> as reported earlier.<sup>55</sup> To Nb 3d levels have binding energies (BE) that range from 208 eV for Nb 3d<sub>3/2</sub> to 212 eV for Nb 3d<sub>5/2</sub> as indicated Fig. 3(b). The spin-orbit splitting energy of 4 eV and the BE numbers are consistent with the

Nb<sup>5+</sup> state.<sup>56</sup> The XPS spectra for S 2p was represented in Fig. 3(c). Peaks at 162.5 and 168.5 eV appeared which belong to S 2p<sub>1/2</sub> and S 2p<sub>3/2</sub>.<sup>57</sup>

### 3.4. Raman spectrometry

The Raman spectroscopy results for Ag<sub>2</sub>S, NbS, and NbAg<sub>2</sub>S nanopowder were recorded using an optimal laser stimulation power of 40 mW (Fig. 3(d)). The high stimulation power resulted in elevated spectral intensity but also caused the photoinduced breakdown of silver sulfide, which caused the emergence of a very strong peak at 1444 cm<sup>−1</sup> and strong peaks at 485 and 1255 cm<sup>−1</sup>. Strong peaks at 485, 1255, and 1444 cm<sup>−1</sup> are caused by vibrations of sulphur oxide molecules and silver metals created by the photoinduced breakdown of Ag<sub>2</sub>S.<sup>58</sup> There are three peaks observed from the Raman spectrum of niobium sulfide. The peak appeared at 151 cm<sup>−1</sup> may be due to some defects.<sup>59</sup> The two peaks at 309 and 389 cm<sup>−1</sup> correspond to the niobium sulfide structure.<sup>60</sup>

### 3.5. EIS and BET measurements

Electrochemical impedance spectroscopy (EIS) uses a wide range of AC frequencies. It determines the electrical resistance (impedance) of the metal/solution interface over a broad frequency series (from 1 MHz to 10 KHz). The well-established quantitative method known as electrochemical impedance spectroscopy can be applied properly to evaluate the anti-corrosion efficiency of protective coatings (EIS). EIS is a valuable tool for investigating the interfacial properties of bio-recognition processes at the electrode surface. EIS data are



frequently assessed by fitting to an identical electrical circuit model. EIS is one of the most popular analytical techniques.<sup>61–66</sup> A unique electrochemical impedance spectroscopy (EIS) analysis based on evolutionary programming has been used to look at the processes that govern the operation of supercapacitors and their decomposition procedures.<sup>67</sup> The EIS graph for NbS, Ag<sub>2</sub>S, and NbAg<sub>2</sub>S was represented in Fig. 4(a–c). The EDLC and faradaic behavior can be observed from the straight line along with the small semicircle. The ESR was also calculated from the EIS graph for NbS, Ag<sub>2</sub>S, and NbAg<sub>2</sub>S. The ESR for NbAg<sub>2</sub>S was 1.04 U, less than NbS (1.13 U) and Ag<sub>2</sub>S (1.18 U).

An analytical method called Brunauer–Emmett–Teller (BET) was used to investigate pore volume and surface area for pure solid materials. In this technique, an inert gas, like nitrogen, is adsorbed onto the solid surface of the sample. The physical adsorption of gas molecules on a pure solid surface is the fundamental basis of an important analytical technique for figuring out the specific surface area of materials. All material was outgassed at 100 °C for 7 h in a vacuum before measurements were taken.<sup>68,69</sup> Using the BET method, the surface area of NbS, Ag<sub>2</sub>S, and NbAg<sub>2</sub>S was calculated and represented in Fig. 4(d–f). BET surface area of the NbS, Ag<sub>2</sub>S, and NbAg<sub>2</sub>S was 24.76, 19.43, and 35.71 m<sup>2</sup> g<sup>−1</sup>, respectively. The porous surface morphologies were useful for energy storage applications because their extensive pore channels enable quick electrolyte

transport, and small holes provide more active sites for chemical reactions.<sup>70,71</sup> According to Brousse *et al.*, who synthesized corresponding mixtures and amorphous ones, BET analysis and water content have no further impact on capacitance.<sup>74</sup>

On the other hand, the capacitance of the Nb-derived sample is unaffected by the increase in BET surface area. Additionally, after the proton exchange operation, the capacitance in the case of NbAg<sub>2</sub>S decreases, raising the BET value. These results showed that the element shape and size determine the capacitance in addition to the BET surface area and the type of the examined part. This outcome aligns with the general findings of Toupin *et al.*<sup>73</sup> Going to prove that in pseudo-capacitive phenomena related to faradaic reactions, the microstructure significantly impacts capacitance levels.<sup>72,74</sup> Fig. 3(d–f) indicates the BET graph for NbS, Ag<sub>2</sub>S, and NbAg<sub>2</sub>S. Table 1 lists the average pore diameters, specific surface areas, and pore volumes of NbS, Ag<sub>2</sub>S, and NbAg<sub>2</sub>S determined by BET measurements. The experiments used composite electrodes, demonstrating a significant difference between the samples.<sup>75</sup>

### 3.6. Electrochemical results

The electrochemical results of NbS, Ag<sub>2</sub>S, and NbAg<sub>2</sub>S were first calculated with the use of a three-electrode assembly. At various scan rates, CV measurements for all prepared materials (NbS, Ag<sub>2</sub>S, and NbAg<sub>2</sub>S) were taken in a 1 M KOH electrolyte at an OP

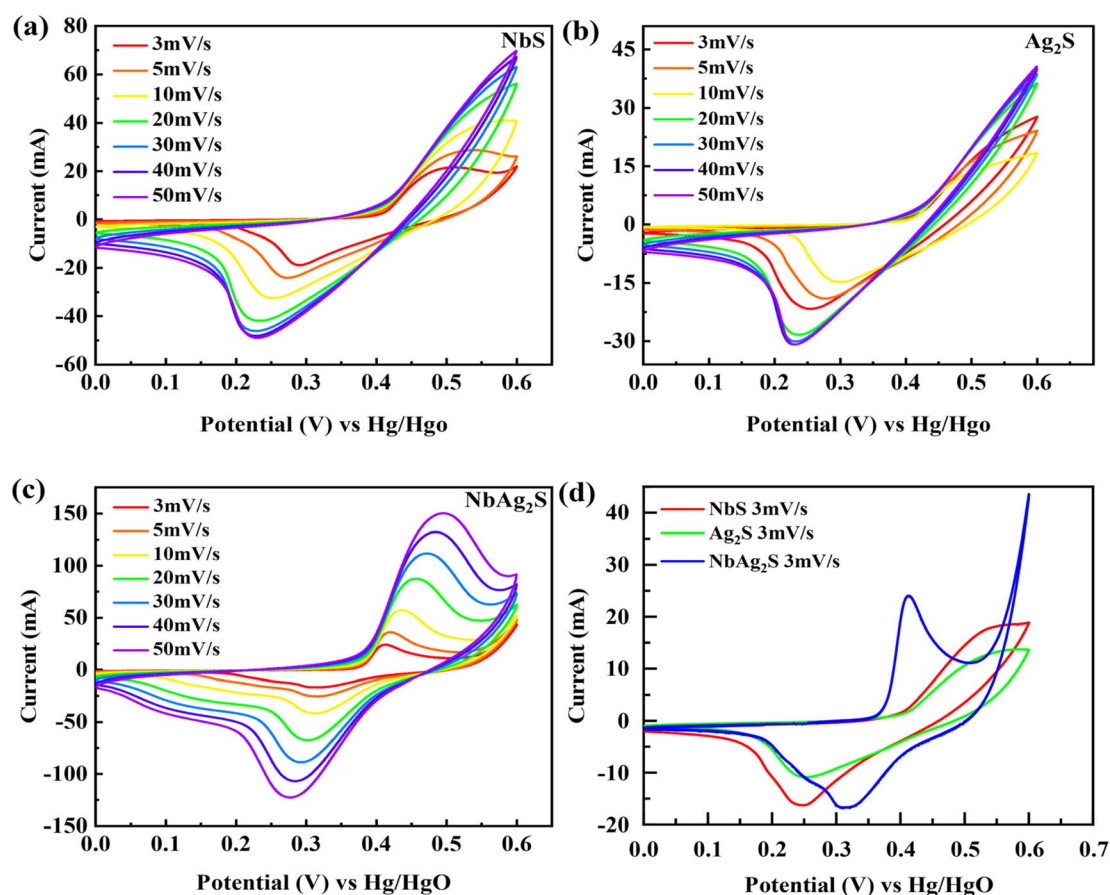


Fig. 5 (a–c) Represents CV graphs for NbS, Ag<sub>2</sub>S, and NbAg<sub>2</sub>S, respectively. (d) CV comparison for NbS, Ag<sub>2</sub>S, and NbAg<sub>2</sub>S at 3 mV s<sup>−1</sup>.

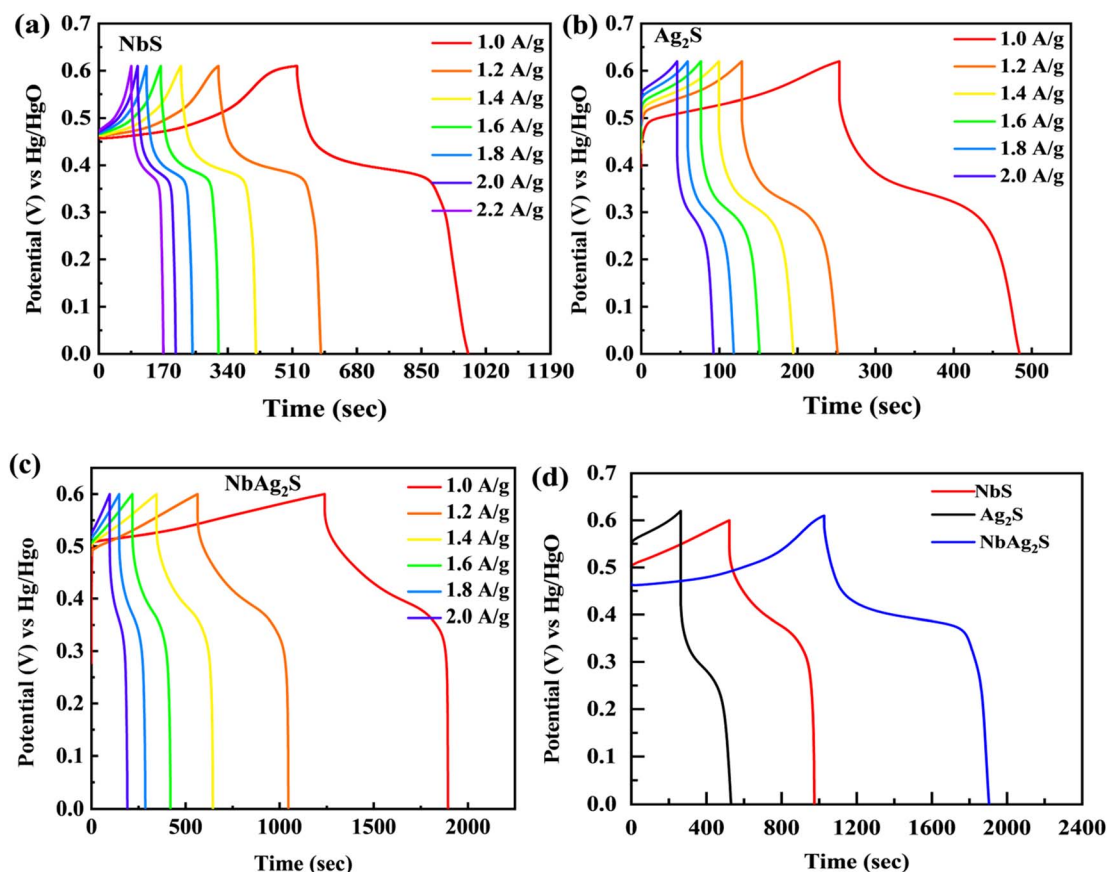


Fig. 6 (a–c) Represents GCD graphs for NbS, Ag<sub>2</sub>S, and NbAg<sub>2</sub>S, respectively. (d) GCD comparison for NbS, Ag<sub>2</sub>S, and NbAg<sub>2</sub>S at 1.0 A g<sup>−1</sup>.

of (0–0.6 V). Fig. 5 displays the CV measurements of NbS, Ag<sub>2</sub>S, and NbAg<sub>2</sub>S. The CV measurements describe the storage mechanism in materials. The CV curves for NbS, Ag<sub>2</sub>S, and NbAg<sub>2</sub>S had nonrectangular shapes that indicate faradaic nature. The faradaic behavior was evidence of the battery-type attitude of NbS, Ag<sub>2</sub>S, and NbAg<sub>2</sub>S. Additionally, the redox peaks increase with the rise in scan rate, further proving the battery-like behavior of NbS, Ag<sub>2</sub>S, and NbAg<sub>2</sub>S. Redox peaks become wider as the scan rate increases.<sup>76–78</sup> NbS had a capacity of 394.4 C g<sup>−1</sup> when calculated through CV using equation no 1, while Ag<sub>2</sub>S had a capacity of 206 C g<sup>−1</sup> at 3 mV s<sup>−1</sup>. The NbS and Ag<sub>2</sub>S are combined to improve overall performance. NbAg<sub>2</sub>S, the final product, had a maximum capacity of 645 C g<sup>−1</sup>. Fig. 5(a–c) displays the CV results for NbS, Ag<sub>2</sub>S, and NbAg<sub>2</sub>S at different scan rates ranging from 3 to 50 mV s<sup>−1</sup>. The synergistic effect of NbS and Ag<sub>2</sub>S, fast movement of ions, and increased surface area result in increased specific capacity of NbSAg<sub>2</sub>S. Fig. 5(d) compares CV curves for NbS, Ag<sub>2</sub>S, and NbAg<sub>2</sub>S at 3 mV s<sup>−1</sup>. The combination of NbS and Ag<sub>2</sub>S increases conductivity and surface area, two important properties for electrochemical measurements. The area under the curve improves as the scan rate increases due to a reduction in the charging/discharging time.<sup>51,79,80</sup> For NbS, Ag<sub>2</sub>S, and NbAg<sub>2</sub>S, the calculated specific capacitance Cs were 657.5, 343.33, and 1075 F g<sup>−1</sup>, respectively. Increased surface area and higher electric conductivity may be due to the synergetic impact of combined NbS and Ag<sub>2</sub>S. The

increased electrochemical performance of NbAg<sub>2</sub>S may be because of the quick exchanges of ions from the electrolyte to the surface.<sup>81,82</sup> Eqn (2) was applied to estimate the capacity for NbS, Ag<sub>2</sub>S, and NbAg<sub>2</sub>S through GCD curves using discharge time. In contrast to the individual NbS and Ag<sub>2</sub>S, the combined NbAg<sub>2</sub>S discharge time was 654 s at 1.0 A g<sup>−1</sup>, which is long, as indicated in Fig. 6(c). The GCD profiles of NbS, Ag<sub>2</sub>S, and NbAg<sub>2</sub>S indicate little deviation from EDLC triangular behavior, which attributes to battery-like attitude. The charging/discharging time decreases as the current density increases. This was due to ions–electrons interaction increases due to higher excitation. The discharge duration for NbS was 440 s at 1.0 A g<sup>−1</sup>, and for Ag<sub>2</sub>S was 232 s at 1.0 A g<sup>−1</sup>, as represented in Fig. 6(a and b). The specific capacities for NbS, Ag<sub>2</sub>S, and NbAg<sub>2</sub>S were estimated from the GCD profiles, and the results displayed that the specific capacities of single NbS and Ag<sub>2</sub>S were lower than NbAg<sub>2</sub>S. NbS had a maximum specific capacity of 440 C g<sup>−1</sup> and a current density of 1.0 A g<sup>−1</sup>. Fig. 6(d) indicates the comparative GCD plot of NbS, Ag<sub>2</sub>S, and NbAg<sub>2</sub>S at 1.0 A g<sup>−1</sup>. The specific capacity for Ag<sub>2</sub>S was 232 C g<sup>−1</sup> at 1.0 A g<sup>−1</sup>. The specific capacity of NbAg<sub>2</sub>S composite material was 654 C g<sup>−1</sup> at 1.0 A g<sup>−1</sup>. The specific capacitance was also measured from GCD graphs. For NbS, Ag<sub>2</sub>S, and NbAg<sub>2</sub>S, the measured capacitance values were 733.33, 386.66, and 1090 F g<sup>−1</sup> at 1.0 A g<sup>−1</sup>, respectively. The composite of niobium and silver was the finest material among all, with a specific capacity



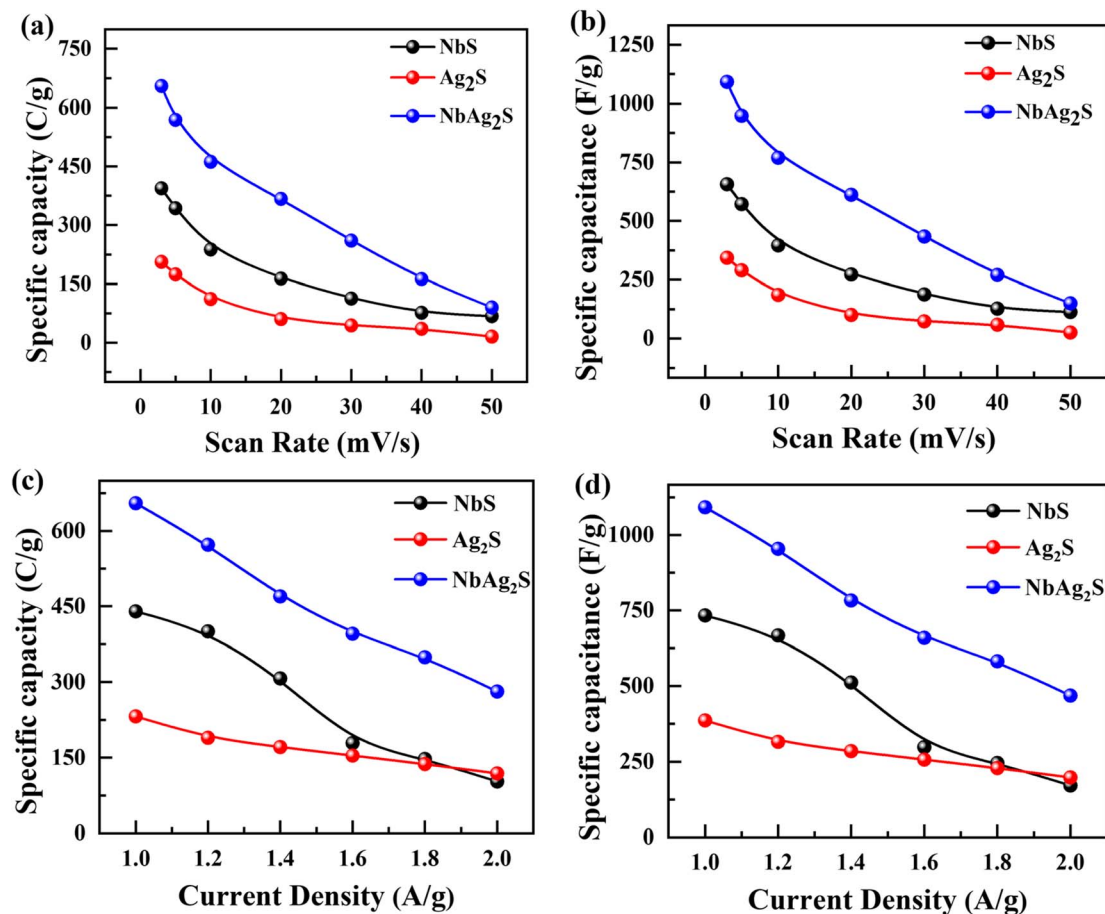


Fig. 7 (a and b) Specific capacity and capacitance for NbS, Ag<sub>2</sub>S, and NbAg<sub>2</sub>S through CV graphs. (c and d) Specific capacity and capacitance for NbS, Ag<sub>2</sub>S, and NbAg<sub>2</sub>S through GCD graphs.

of 654 C g<sup>-1</sup> in GCD measurements. This implies that, in contrast to individual Ag<sub>2</sub>S and NbS, combined NbAg<sub>2</sub>S was more active and, as a result, the movement of ions and electrons is much simpler. The increased surface area and improved conductivity of NbAg<sub>2</sub>S were also linked to more active spots. The specific capacity and capacitance for NbS, Ag<sub>2</sub>S, and NbAg<sub>2</sub>S were shown in Fig. 7. The large surface area, number of active sites, exposed ion transfer region, less recombination, and small size of particles were responsible for the enhanced performance of NbAg<sub>2</sub>S.<sup>51</sup> This NbAg<sub>2</sub>S candidate, therefore, has tremendous potential for supercapacitor applications.

### 3.7. Two electrode assembly

The best material (NbAg<sub>2</sub>S) was selected for two-cell operation with activated carbon (AC) to develop supercapattery. An asymmetric device was developed with (AC) as the negative electrode and NbAg<sub>2</sub>S as the positive electrode, as displayed in Fig. 8(a). The CV measurements for AC and NbAg<sub>2</sub>S were performed separately using a three-electrode assembly, as shown in Fig. 8(b). The CV and GCD calculations for the NbAg<sub>2</sub>S//AC device were indicated in Fig. 8(c and d).

Supercapacitors should operate at a large operating potential (OP) to achieve maximum energy density. Fig. 8(c) represents

the CV measurements for NbAg<sub>2</sub>S//AC in a two-electrode assembly at various scan rates between 3–100 mV s<sup>-1</sup> in a 1 M solution of KOH. The OP for NbAg<sub>2</sub>S//AC supercapattery was 0–1.6 V due to the combined OP of AC (–1 to 0 V) and NbAg<sub>2</sub>S (0–0.6 V). The rectangular form of CV graphs was evidence of the capacitive nature of AC. The virtually rectangular form of CV profiles for NbAg<sub>2</sub>S//AC device at 0–0.5 V potential indicates a capacitive attitude. Little redox peaks that indicated faradaic reactions appeared at the potential from 0.5 V to 1.6 V. At higher scans, the CV form does not alter, demonstrating the overall stability and higher rate capability of the NbAg<sub>2</sub>S//AC device. Similarly, GCD was carried out in an electrolyte of 1 M KOH with OP of 0 V to 1.6 V. The results of the GCD calculations were displayed in Fig. 8(d). The almost triangular shapes of the GCD curves with the small highland region support our assumption of the formation of supercapattery. The GCD curves indicate the EDLC and pseudo-capacitive behavior. The specific capacity of the NbAg<sub>2</sub>S//AC hybrid device was also determined from CV and GCD, as indicated in Fig. 9(a and b). The capacity of the NbAg<sub>2</sub>S//AC hybrid device calculated from CV was 112.8 C g<sup>-1</sup>, while 142 C g<sup>-1</sup> from GCD. When the current density reached 2 A g<sup>-1</sup>, the capacity reduces to 25.06 C g<sup>-1</sup>. This device was offered for 5000 charging/discharging cycles for





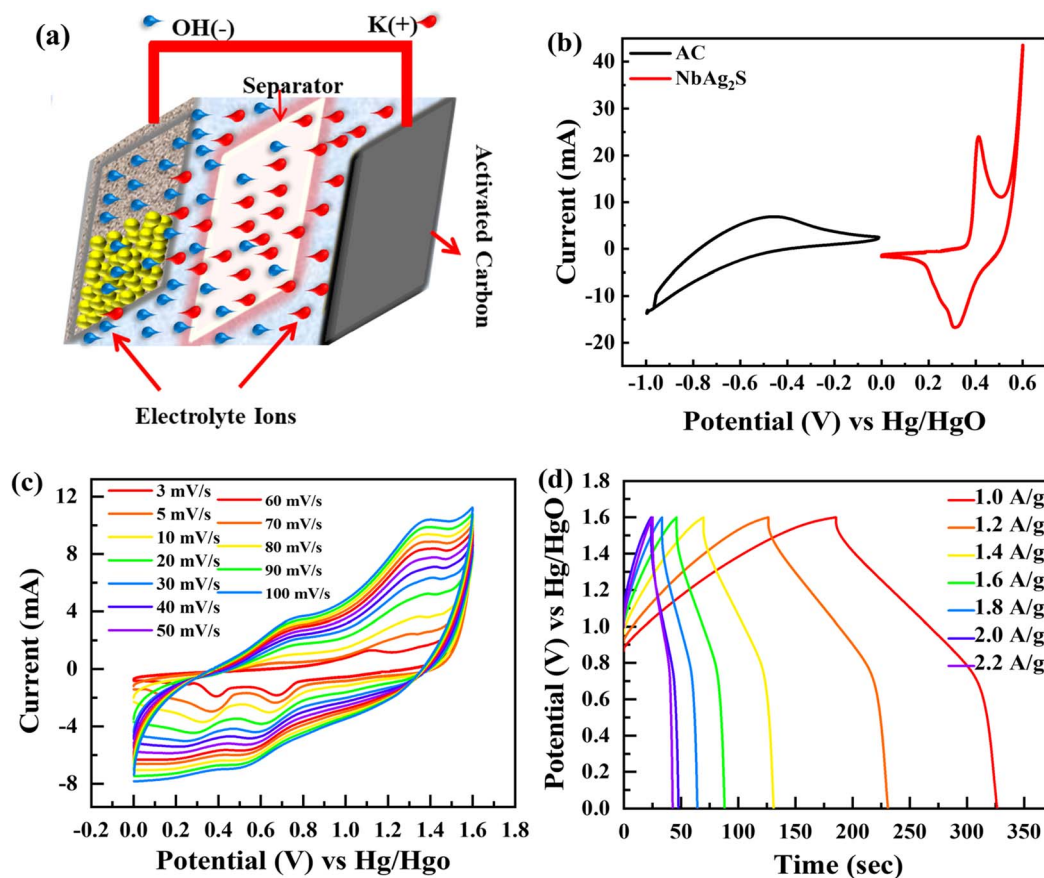


Fig. 8 (a) Systematic image of NbAg<sub>2</sub>S//AC supercapattery. (b) CV comparison of AC and NbAg<sub>2</sub>S. (c) CV curves for NbAg<sub>2</sub>S//AC supercapattery at different scans. (d) GCD curves for NbAg<sub>2</sub>S//AC supercapattery at different scan rates.

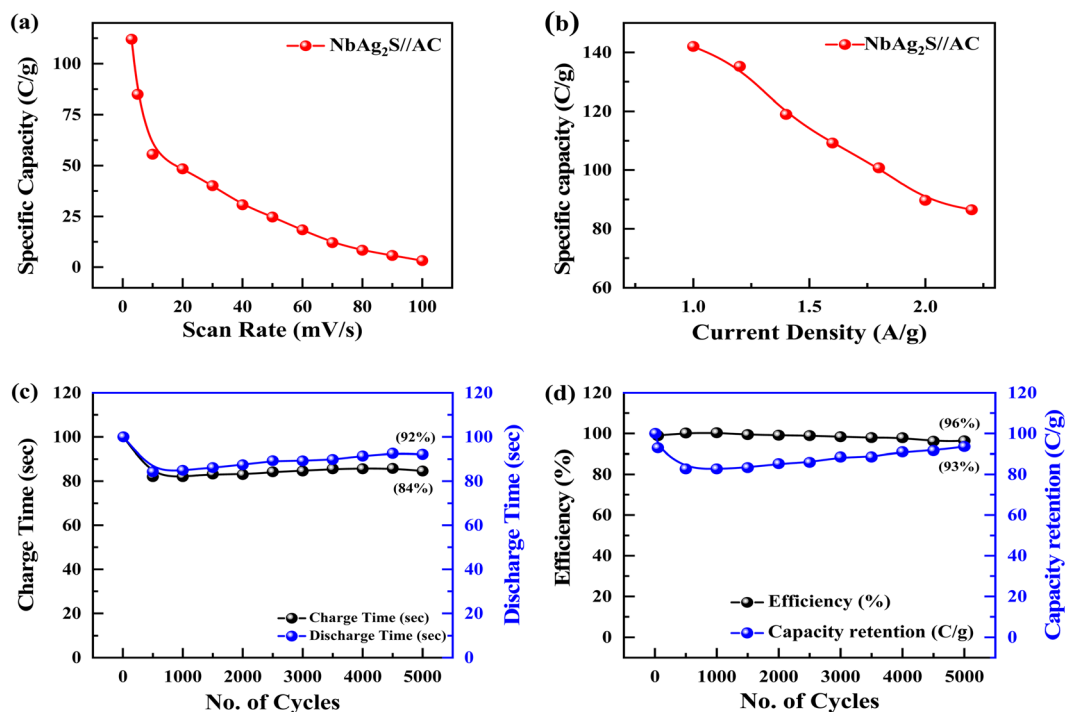


Fig. 9 (a and b) Specific capacity of NbAg<sub>2</sub>S//AC supercapattery through CV and GCD. (c and d) Charge/Discharge time and coulombic efficiency/capacity retention measured for NbAg<sub>2</sub>S//AC supercapattery after 5000 cycles.



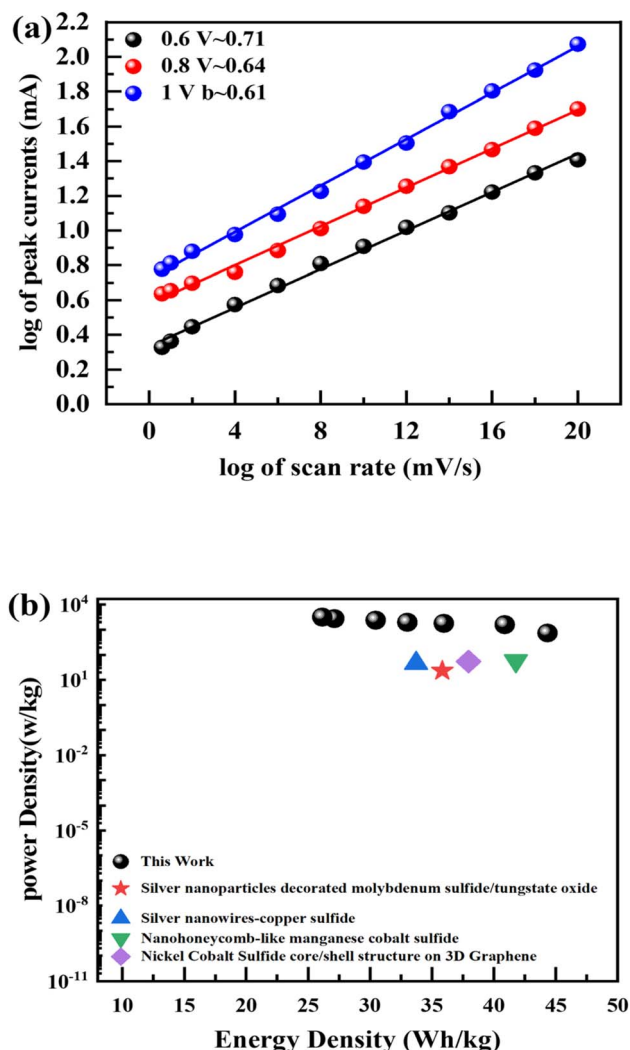


Fig. 10 (a)  $b$ -Fitting computed for NbAg<sub>2</sub>S//AC supercapattery. (b) Energy density and power density computed for NbAg<sub>2</sub>S//AC supercapattery.

Table 2 Represents the comparison of  $E_d$  and  $P_d$  of NbAg<sub>2</sub>S//AC supercapattery with past work

Energy density (W h kg <sup>-1</sup> )	Power density (W kg <sup>-1</sup> )	Previous study
10.01	520	AgCuS core/shell <sup>83</sup>
18.4	254.5	Ni-Co-S nano-sheets <sup>84</sup>
28.22	596	2D vanadium disulfide/black phosphorus hybrids <sup>85</sup>
25.71	8.73	CoZnS/Cu <sub>2</sub> O <sub>3</sub> nanoarrays <sup>86</sup>
25.71	8.73	Cobalt zinc sulfide/copper oxide nanoarrays <sup>86</sup>
19.63	340	Ag-MoS/WS <sub>2</sub> (ref. 87)
43.06	750	<b>This work</b>

a supercapattery lifecycle test. Fig. 9(c and d) indicates stability performance after 5000 cycles. The charge/discharge time was shown in Fig. 9(c) against 5000 cycles. The blue curve in Fig. 9(d)

depicts the capacity retention of this device after 5000 cycles, which is still 93%. While the red curve in Fig. 9(d) indicates that coulombic efficiency which was 96.35% after 5000 cycles. The  $b$ -fitting was also computed to support our hypothesis of supercapattery development. The charge storage in the NbAg<sub>2</sub>S//AC device was essentially determined using  $b$  values. Fig. 10(a) displays the estimated  $b$ -values of the NbAg<sub>2</sub>S//AC device at several potentials. The  $b$ -values range for a battery lies between 0–0.5, while that of a supercapacitor was 0.8–1.0, and that of a supercapattery was between 0.5–0.8.<sup>79</sup> The calculated  $b$ -values, therefore, fall within the range of supercapattery, as shown in Fig. 10(a). Thus the storage mechanism in the NbAg<sub>2</sub>S//AC device was a fusion of both capacitive and faradaic reactions. Eqn (3) and (4) were used to calculate energy and power densities. At 1.0 A g<sup>-1</sup> current density, the supercapattery (NbAg<sub>2</sub>S//AC) delivers 43.06 W h kg<sup>-1</sup> energy while upholding a power density of 750 W kg<sup>-1</sup>. Fig. 10(b) compares the energy density to the previously reported work. Table 2 represented the comparison of this work with previous reports. We also calculated the capacitive and diffusive part in the ESI portion (Fig. S1†).

The combination of NbS and Ag<sub>2</sub>S had a 50/50 weight ratio (NbAg<sub>2</sub>S) offering good potential for future applications in (ESD) energy storage devices.

## 4. Conclusion

The hydrothermal technique was used in this study to synthesize NbS, Ag<sub>2</sub>S, and NbAg<sub>2</sub>S for supercapattery applications. SEM and XRD were used to study the physical structure and surface morphology of the NbS, Ag<sub>2</sub>S, and NbAg<sub>2</sub>S. The NbAg<sub>2</sub>S showed higher values of the specific capacity as compared to NiS and Ag<sub>2</sub>S due to greater surface area and high electronic mobility. The composite NbAg<sub>2</sub>S had a capacity of 654 C g<sup>-1</sup> at 1.0 A g<sup>-1</sup> current. The NbAg<sub>2</sub>S was also used as anode material in a supercapattery (NbAg<sub>2</sub>S//AC). The capacity of 142 C g<sup>-1</sup> at 1.0 A g<sup>-1</sup> was achieved in a two-electrode assembly for the NbAg<sub>2</sub>S//AC device. The supercapattery NbAg<sub>2</sub>S//AC provided an energy density of 43.06 W h kg<sup>-1</sup> at 750 W kg<sup>-1</sup> power. After 5000 cycles of charging and discharging, the coulombic efficiency of the NbAg<sub>2</sub>S//AC hybrid device was 96%. The NbAg<sub>2</sub>S as an electrode material for asymmetric devices will perform better in the future.

## Conflicts of interest

There are no conflicts to declare.

## Acknowledgements

The authors are grateful to the Researchers Supporting Project Number (RSP2023R448), King Saud University, Riyadh, Saudi Arabia.

## References

- G. Quartey and S. K. Adzimah, *J. Exp. Theor. Phys.*, 2014, **4**, 19.



- 2 Y. Zhang, J. Wei, Y. Zhu and G. George-Ufot, *J. Cleaner Prod.*, 2020, **263**, 121584.
- 3 J. P. Sidhu, W. Ahmed, W. Gernjak, R. Aryal, D. McCarthy, A. Palmer, P. Kolotelo and S. Toze, *Sci. Total Environ.*, 2013, **463**, 488–496.
- 4 S. Saint Akadiri, A. A. Alola, G. Olasehinde-Williams and M. U. Etokakpan, *Sci. Total Environ.*, 2020, **708**, 134653.
- 5 L. L. Zhang and X. Zhao, *Chem. Soc. Rev.*, 2009, **38**, 2520–2531.
- 6 Q. Lu, M. W. Lattanzi, Y. Chen, X. Kou, W. Li, X. Fan, K. M. Unruh, J. G. Chen and J. Q. Xiao, *Angew. Chem., Int. Ed.*, 2011, **50**, 6847–6850.
- 7 H. Wang, C. Zhu, D. Chao, Q. Yan and H. J. Fan, *Adv. Mater.*, 2017, **29**, 1702093.
- 8 J. Qin, V. P. Pasko, M. G. McHarg and H. C. Stenbaek-Nielsen, *Nat. Commun.*, 2014, **5**, 1–6.
- 9 A. Marins, S. Banhos, E. Muri, R. Rodrigues, P. Cruz and M. Freitas, *Mater. Chem. Phys.*, 2020, **242**, 122440.
- 10 N. J. Vickers, *Curr. Biol.*, 2017, **27**, R713–R715.
- 11 A. S. Brierley, P. G. Fernandes, M. A. Brandon, F. Armstrong, N. W. Millard, S. D. McPhail, P. Stevenson, M. Pebody, J. Perrett and M. Squires, *Science*, 2002, **295**, 1890–1892.
- 12 J. R. Miller and A. Burke, *Electrochem. Soc. Interface*, 2008, **17**, 53.
- 13 F. Wang, S. Xiao, Y. Zhu, Z. Chang, C. Hu, Y. Wu and R. Holze, *J. Power Sources*, 2014, **246**, 19–23.
- 14 F. S. Omar, A. Numan, N. Duraisamy, S. Bashir, K. Ramesh and S. Ramesh, *RSC Adv.*, 2016, **6**, 76298–76306.
- 15 H. Jiang, J. Sun, L. Wei, M. Wu, W. Shyy and T. Zhao, *Energy Storage Mater.*, 2020, **24**, 529–540.
- 16 H. Kim, M. Ramalingam, V. Balakumar, X. Zhang, W. Gao, Y.-A. Son and P. D. Bradford, *Chem. Phys. Lett.*, 2020, **739**, 136957.
- 17 D. Potphode and C. S. Sharma, *J. Energy Storage*, 2020, **27**, 101114.
- 18 G. Z. Chen, *Int. Mater. Rev.*, 2017, **62**, 173–202.
- 19 A. Chandra, *Proc. Natl. Acad. Sci., India, Sect. A*, 2012, **82**, 79–90.
- 20 S. Roldán, D. Barreda, M. Granda, R. Menéndez, R. Santamaría and C. Blanco, *Phys. Chem. Chem. Phys.*, 2015, **17**, 1084–1092.
- 21 N. Muzaffar, A. M. Afzal, H. Hegazy and M. W. Iqbal, *J. Energy Storage*, 2023, **64**, 107142.
- 22 G.-L. Xu, Y.-D. Gong, C. Miao, Q. Wang, S.-Q. Nie, Y. Xin, M.-Y. Wen, J. Liu and W. Xiao, *Rare Met.*, 2022, **41**, 3421–3431.
- 23 W. Grosshans and W. Holzapfel, *Phys. Rev. B: Condens. Matter Mater. Phys.*, 1992, **45**, 5171.
- 24 W. Shimizu, S. Makino, K. Takahashi, N. Imanishi and W. Sugimoto, *J. Power Sources*, 2013, **241**, 572–577.
- 25 S. Makino, Y. Shinohara, T. Ban, W. Shimizu, K. Takahashi, N. Imanishi and W. Sugimoto, *RSC Adv.*, 2012, **2**, 12144–12147.
- 26 D. Hu, C. Peng and G. Z. Chen, *ACS Nano*, 2010, **4**, 4274–4282.
- 27 B. Akinwolemiwa, C. Peng and G. Z. Chen, *J. Electrochem. Soc.*, 2015, **162**, A5054.
- 28 D. S. Su and G. Centi, *J. Energy Chem.*, 2013, **22**, 151–173.
- 29 A. Krueger, *Chem.-Eur. J.*, 2008, **14**, 1382–1390.
- 30 M. Imran, A. M. Afzal, M. W. Iqbal, H. Hegazy, M. Z. Iqbal, S. Mumtaz and R. Qureshi, *Mater. Sci. Semicond. Process.*, 2023, **158**, 107366.
- 31 S. Chandrasekaran, L. Yao, L. Deng, C. Bowen, Y. Zhang, S. Chen, Z. Lin, F. Peng and P. Zhang, *Chem. Soc. Rev.*, 2019, **48**, 4178–4280.
- 32 X. Rui, H. Tan and Q. Yan, *Nanoscale*, 2014, **6**, 9889–9924.
- 33 A. Borenstein, O. Hanna, R. Attias, S. Luski, T. Brousse and D. Aurbach, *J. Mater. Chem. A*, 2017, **5**, 12653–12672.
- 34 Y. Shao, M. F. El-Kady, J. Sun, Y. Li, Q. Zhang, M. Zhu, H. Wang, B. Dunn and R. B. Kaner, *Chem. Rev.*, 2018, **118**, 9233–9280.
- 35 Z. S. Iro, C. Subramani and S. Dash, *Int. J. Electrochem. Sci.*, 2016, **11**, 10628–10643.
- 36 J. S. Sanchez, A. Pendashteh, J. Palma, M. Anderson and R. Marcilla, *J. Mater. Chem. A*, 2019, **7**, 20414–20424.
- 37 L. Xu, L. Ma, T. Rujiralai, X. Zhou, S. Wu and M. Liu, *RSC Adv.*, 2017, **7**, 33937–33943.
- 38 X. Shang, J.-Q. Chi, S.-S. Lu, J.-X. Gou, B. Dong, X. Li, Y.-R. Liu, K.-L. Yan, Y.-M. Chai and C.-G. Liu, *Appl. Surf. Sci.*, 2017, **392**, 708–714.
- 39 H. Hegazy, A. M. Afzal, E. Shaaban, M. W. Iqbal, S. Muhammad and A. Alahmari, *Ceram. Int.*, 2023, **49**, 1710–1719.
- 40 C. Altavilla, M. Sarno and P. Ciambelli, *Chem. Mater.*, 2011, **23**, 3879–3885.
- 41 X. Ou, X. Xiong, F. Zheng, C. Yang, Z. Lin, R. Hu, C. Jin, Y. Chen and M. Liu, *J. Power Sources*, 2016, **325**, 410–416.
- 42 W. Li, X. Wei, H. Dong, Y. Ou, S. Xiao, Y. Yang, P. Xiao and Y. Zhang, *Front. Chem.*, 2020, **8**, 189.
- 43 M. Danot, J. Afonso, J. Portefaix, M. Breyse and T. Des Courières, *Catal. Today*, 1991, **10**, 629–643.
- 44 S. A. Pawar, D. S. Patil and J. C. Shin, *Electrochim. Acta*, 2018, **259**, 664–675.
- 45 A. M. Awwad, N. M. Salem, M. M. Aqarbeh and F. M. Abdulaziz, *Chem. Int.*, 2020, **6**, 42–48.
- 46 T. Abbas, M. W. Iqbal, S. Gouadria, H. Hegazy, H. u. Hassan, A. M. Afzal, S. Aftab and A. Alzahrani, *J. Solid State Electrochem.*, 2023, 1–11.
- 47 S. A. Pawar, D. S. Patil and J. C. Shin, *ChemElectroChem*, 2019, **6**, 522–534.
- 48 S. Vijayakumar, S. Nagamuthu and G. Muralidharan, *ACS Appl. Mater. Interfaces*, 2013, **5**, 2188–2196.
- 49 F. S. Omar, A. Numan, N. Duraisamy, M. M. Ramly, K. Ramesh and S. Ramesh, *Electrochim. Acta*, 2017, **227**, 41–48.
- 50 M. Z. Iqbal, A. Khan, A. Numan, S. S. Haider and J. Iqbal, *Ultrason. Sonochem.*, 2019, **59**, 104736.
- 51 M. Z. Iqbal, M. M. Faisal, S. R. Ali, A. M. Afzal, M. R. A. Karim, M. A. Kamran and T. Alharbi, *Ceram. Int.*, 2020, **46**, 10203–10214.
- 52 A. Lawson, *Mater. Res. Bull.*, 1972, **7**, 1–8.
- 53 G. Yang, X. Zhao, F. Liao, Q. Cheng, L. Mao, H. Fa and L. Chen, *Sustainable Energy Fuels*, 2021, **5**, 3039–3083.



- 54 X. Sun, B. Shi, H. Wang, N. Lin, S. Liu, K. Yang, B. Zhang and J. He, *Adv. Opt. Mater.*, 2020, **8**, 1901181.
- 55 V. A. Kumar, T. Uchida, T. Mizuki, Y. Nakajima, Y. Katsube, T. Hanajiri and T. Maekawa, *Adv. Nat. Sci.: Nanosci. Nanotechnol.*, 2016, **7**, 015002.
- 56 M. Lübke, J. Shin, P. Marchand, D. Brett, P. Shearing, Z. Liu and J. A. Darr, *J. Mater. Chem. A*, 2015, **3**, 22908–22914.
- 57 M. Fantauzzi, B. Elsener, D. Atzei, A. Rigoldi and A. Rossi, *RSC Adv.*, 2015, **5**, 75953–75963.
- 58 S. Sadovnikov, E. Vovkotrub and A. Rempel, *Dokl. Phys. Chem.*, 2018, **480**, 81–84.
- 59 W. Ge, K. Kawahara, M. Tsuji and H. Ago, *Nanoscale*, 2013, **5**, 5773–5778.
- 60 Q. Lv, X. Qin and R. Lv, *Frontiers in Materials*, 2019, **6**, 279.
- 61 J. Macdonald, *Int. Soc. Work*, 1987, 150–170.
- 62 C. Gabrielli, *Electrochim. Acta*, 2020, **331**, 135324.
- 63 C. Gabrielli, *Science*, 1998, 1–120.
- 64 R. De Levie, *Adv. Electrochem. Electrochem. Eng.*, 1967, **6**, 329–397.
- 65 R. Kötz and M. Carlen, *Electrochim. Acta*, 2000, **45**, 2483–2498.
- 66 P. Kurzweil and H.-J. Fischle, *J. Power Sources*, 2004, **127**, 331–340.
- 67 G. A. Ali, O. A. Fouad, S. A. Makhlof, M. M. Yusoff and K. F. Chong, *J. Solid State Electrochem.*, 2014, **18**, 2505–2512.
- 68 M. Aghazadeh, *J. Appl. Electrochem.*, 2012, **42**, 89–94.
- 69 E. Elanthamilan, B. C. Meena, N. Renuka, M. Santhiya, J. George, E. Kanimozhi, J. C. Ezhilarasi and J. P. Merlin, *J. Electroanal. Chem.*, 2021, **901**, 115762.
- 70 P. Simon and Y. Gogotsi, in *Nanoscience and technology: a collection of reviews from Nature journals*, World Scientific, 2010, pp. 320–329.
- 71 J. Yang, P. Xiong, C. Zheng, H. Qiu and M. Wei, *J. Mater. Chem. A*, 2014, **2**, 16640–16644.
- 72 E. Beaudrouet, A. L. G. La Salle and D. Guyomard, *Electrochim. Acta*, 2009, **54**, 1240–1248.
- 73 A. M. Moseley, P. Rahman, G. A. Wells, J. R. Zadro, C. Sherrington, K. Toupin-April and L. Brosseau, *PLoS One*, 2019, **14**, e0222770.
- 74 M. Toupin, T. Brousse and D. Bélanger, *Chem. Mater.*, 2002, **14**, 3946–3952.
- 75 M. Toupin, D. Bélanger, I. R. Hill and D. Quinn, *J. Power Sources*, 2005, **140**, 203–210.
- 76 M. Jin, S.-Y. Lu, L. Ma, M.-Y. Gan, Y. Lei, X.-L. Zhang, G. Fu, P.-S. Yang and M.-F. Yan, *J. Power Sources*, 2017, **341**, 294–301.
- 77 P. Simon, Y. Gogotsi and B. Dunn, *Science*, 2014, **343**, 1210–1211.
- 78 M. F. Iqbal, M. N. Ashiq, A. Razaq, M. Saleem, B. Parveen and M.-U. Hassan, *Electrochim. Acta*, 2018, **273**, 136–144.
- 79 M. Z. Iqbal, M. M. Faisal, S. R. Ali, S. Farid and A. M. Afzal, *Electrochim. Acta*, 2020, **346**, 136039.
- 80 M. Z. Iqbal, M. M. Faisal, S. R. Ali and A. M. Afzal, *J. Electroanal. Chem.*, 2020, **871**, 114299.
- 81 M. F. Iqbal, M. N. Ashiq, S. Iqbal, N. Bibi and B. Parveen, *Electrochim. Acta*, 2017, **246**, 1097–1103.
- 82 H. Hassan, M. W. Iqbal, A. M. Afzal, M. Asghar and S. Aftab, *J. Solid State Electrochem.*, 2023, **27**, 125–137.
- 83 W. Alshammari, D. S. Patil, S. A. Pawar and J. C. Shin, *Mater. Today Chem.*, 2017, **5**, 72–80.
- 84 S. Xu, C. Su, T. Wang, Y. Ma, J. Hu, J. Hu, N. Hu, Y. Su, Y. Zhang and Z. Yang, *Electrochim. Acta*, 2018, **259**, 617–625.
- 85 A. Sharma, S. Kapse, A. Verma, S. Bisoyi, G. K. Pradhan, R. Thapa and C. S. Rout, *ACS Appl. Energy Mater.*, 2022, **5**, 10315–10327.
- 86 K. Liang, J. DeNaufville, A. Jacobson, R. Chianelli and F. Betts, *J. Non-Cryst. Solids*, 1980, **35**, 1249–1254.
- 87 M. B. Poudel, H. P. Karki and H. J. Kim, *J. Energy Storage*, 2020, **32**, 101693.

